

# The role of superheating in the formation of Glass Mountain obsidians (Long Valley, CA) inferred through crystallization of sanidine

Laura E. Waters<sup>1</sup> · Benjamin J. Andrews<sup>1</sup>

Received: 22 February 2016 / Accepted: 10 August 2016 / Published online: 3 September 2016  
© Springer-Verlag Berlin Heidelberg 2016

**Abstract** The Glass Mountain obsidians (Long Valley, CA) are crystal poor (<8 vol%) and highly evolved (high SiO<sub>2</sub>, low Sr), and therefore, their formation required extremely efficient separation of melts from a crystal-rich source. A petrologic and experimental investigation of the mineral phases in Glass Mountain lavas identifies conditions under which phenocrysts grew and the driving mechanism for crystallization, which places constraints on the possible processes that generated the obsidians. The obsidian in this study (GM-11) is saturated in nine phases (sanidine + quartz + plagioclase + titanomagnetite + ilmenite + zircon + apatite + allanite + biotite), and results of high-resolution SEM compositional mapping and electron microprobe analysis reveal that individual sanidine crystals are normally zoned and span a range of compositions (Or<sub>40–78</sub>). Sanidines have a “granophyric” texture, characterized by intergrowths of quartz and sanidine. Mineral phases in the natural sample are compared to H<sub>2</sub>O-saturated phase equilibrium experiments conducted in cold-seal pressure vessels, over a range of conditions (700–850 °C; 75–225 MPa), and all are found to be plausible phenocrysts. Comparison of sanidine compositions from the natural sample with those grown in phase equilibrium

experiments demonstrates that sanidine in the natural sample occurs in a reduced abundance. Further comparison with phase equilibrium experiments suggests that sanidine compositions track progressive loss of dissolved melt water ( $\pm$ cooling), suggesting that crystallization in the natural obsidian was driven predominantly by degassing resulting from decompression. It is paradoxical that an effusively (slowly) erupted lava should contain multiple phenocryst phases, including sanidine crystals that span a range of compositions with granophyric textures, and yet remain so crystal poor. To resolve this paradox, it is necessary that the solidification mechanism (degassing or cooling) that produced the sanidine crystals (and other mineral phases) must have an associated kinetic effect(s) that efficiently hinders crystal nucleation and growth. Decompression experiments conducted in this study and from the literature collectively demonstrate that the simplest way to inhibit nucleation during degassing-induced crystallization is to initiate degassing  $\pm$  cooling from superliquidus conditions, and therefore, the Glass Mountain obsidians were superheated prior to crystallization.

**Keywords** Obsidian · Rhyolite · Sanidine · Crystallization · Superheating · Long Valley

Communicated by Gordon Moore, Ph.D..

**Electronic supplementary material** The online version of this article (doi:10.1007/s00410-016-1291-3) contains supplementary material, which is available to authorized users.

✉ Laura E. Waters  
watersl@si.edu

<sup>1</sup> Department of Mineral Science, National Museum of Natural History, Smithsonian Institution, 10th St. & Constitution Ave. NW, Washington, DC 20560, USA

## Introduction

Long Valley, CA, a basin positioned on the western most margin of Basin and Range extension, is a classic setting for studying the evolution of large-volume, silica-rich systems. The literature provides comprehensive documentation of the geochemical (Bailey 1989; Hildreth 1977, 1979; Metz and Mahood 1985, 1991; Hildreth 2004; Hildreth and Wilson 2007), isotopic (Halliday et al. 1989; Mankinen

et al. 1986; Davies et al. 1994; Simon and Reid 2005) and volatile (Wallace et al. 1999; Anderson et al. 2000) evolution of the silicic system that lies beneath Long Valley. Extensive geologic mapping (Bailey 1989; Metz and Bailey 1993) and age dating studies (e.g., Metz and Mahood 1985; Mankinen et al. 1986) show that the oldest rhyolites (2.1–0.9 Ma; Metz and Mahood 1991) associated with the Long Valley region, which pre-date the cataclysmic eruption of the Bishop Tuff (0.76 Ma; Bailey 1989), are the low-temperature (<725 °C), highly evolved, crystal-poor ( $\leq 8$  vol%; Metz and Mahood 1991) obsidians that form the Glass Mountain edifice (Fig. DR-1).

The Glass Mountain obsidians were the subjects of a debate surrounding the origins of highly evolved liquids (i.e., elevated Rb/Sr ratios; Halliday et al. 1989) as their formation must fundamentally require extensive fractionation of crystalline phases, as well as an extremely efficient melt extraction mechanism. Isotopic evidence presented in Halliday et al. (1989) was proposed to demonstrate that the liquids that formed Glass Mountain were the residual liquids left after extensive crystallization of a large volume of melt. The isotopic results from Halliday et al. (1989), and later Davies et al. (1994), suggested that the obsidian melts were stored as liquids, for a prolonged period ( $10^5$ – $10^6$  y) in the upper crust. An alternative interpretation for the obsidians was presented by Sparks et al. (1990), where it was suggested that the Glass Mountain obsidians were formed as partial melts of pre-existing crust, due to the compositional and isotopic diversity of melt compositions in spatially proximal vents. The hypothesis of Halliday et al. (1989) contrasts dramatically with that of Sparks et al. (1990), as the former requires that highly evolved rhyolites form through the prolonged cooling and crystallization of a large volume of magma (i.e., retrograde processes), leading to long residence times in the crust, as recorded by the isotopes, whereas the latter hypothesis suggests that highly evolved liquids may form by partial melting (i.e., prograde processes), leading to ephemeral residence in the crust and complex isotopic signatures. These studies provided a powerful dataset for the discussion of the plausible timescales (ephemeral or long-lived) over which highly evolved rhyolite magmas reside in the crust, which carries implications for the speeds at which planetary differentiation occurs.

More recently, Simon and Reid (2005) reinvestigate the ages of the Glass Mountain lavas with a variety of isotopic systems (U-series, Nd–Sm, Sr–Rb) in whole rock, glasses, feldspars and zircons. They conclude that the Sr–Rb isotopes within Glass Mountain obsidians reflect relatively rapid differentiation events, rather than prolonged storage; they do not, however, place any constraint on whether or not the differentiation events that produced the highly evolved rhyolites of Glass Mountain were retrograde or prograde.

An additional complexity to the Glass Mountain lavas is that they are obsidian, which means that they erupt effusively (slowly), undergoing nearly complete degassing, yet they have remarkably low crystallinities, resulting in eruptive products consisting of mostly glass. The paradoxical nature of obsidian was initially addressed in a study of degassing-induced plagioclase crystallization (Waters et al. 2015), where it was demonstrated that the most efficient way to hinder extensive plagioclase crystallization is to initiate decompression/cooling from superliquidus conditions. The conclusions of Waters et al. (2015) suggest that an interval of superheating, a period of time above the liquidus long enough to eliminate nucleation sites, is required in order for a liquid to erupt slowly, yet have minimal crystallization. We hypothesize that a period of superheating is also required for the Glass Mountain lavas; however, in order to test this hypothesis, the conditions under which crystallization occurred in the obsidians must be identified.

The crystallization conditions can be estimated by applying model geothermometers (e.g., Buddington and Lindsley 1964; Ghiorso and Evans 2008) and hygrometers (e.g., Housh and Luhr 1991; Putirka 2005; Lange et al. 2009; Waters and Lange 2013) to the mineral assemblages of the Glass Mountain lavas (as in Metz and Mahood 1991). Pre-eruptive temperatures for the Glass Mountain lavas determined from two iron–titanium oxides and the model of Carmichael (1967) and Buddington and Lindsley (1964) are presented in Metz and Mahood (1991) and range from 695 to 788 °C. Metz and Mahood (1991) also present estimates of pre-eruptive H<sub>2</sub>O contents of 2.5–5.7 wt% using a method presented in Hildreth (1977) that incorporates the geochemical activities of the mineral assemblage (biotite + titanomagnetite + sanidine), temperature and oxygen fugacity as recorded by iron oxides (see Hildreth 1977 for specific method details). Results from the natural sample suggest crystallization of the mineral phases occurred under cold, hydrous conditions; however, no driving mechanism for crystallization (cooling or degassing) is presented.

Here, we conduct a petrologic and experimental study to investigate the conditions under which sanidine crystallized in the Glass Mountain obsidians, to determine the driving mechanism for crystallization, and evaluate the possible role of superheating in the formation of the obsidians. We apply our conclusions to refine the existing models for the origins of the Glass Mountain obsidians (i.e., Halliday et al. 1989; Sparks et al. 1990; Mahood 1990) and attempt to resolve which of the scenarios is more likely in the context of the kinetic results of this study. Lastly, by addressing the origins of the mineral assemblages in the Glass Mountain obsidians in the Long Valley region, we also provide new criteria for the possible scenarios under which these highly evolved melts were extracted (separated) from their sources.

**Table 1** Whole rock, groundmass glass and experimental starting composition

	GM-11 whole rock <sup>a</sup>	Gdms glass <sup>b</sup>	$\pm 2\sigma$	Sanidine melt boundary <sup>c</sup>	$\pm 2\sigma$	Exp starting glass <sup>d</sup>	$\pm 2\sigma$
Lat (N)	37° 49.390						
Long (W)	118° 45.006						
SiO <sub>2</sub>	76.2	77.3	1.28	79.3	1.24	76.5	1.24
TiO <sub>2</sub>	0.08	0.07	0.07	0.04	0.07	0.09	0.05
Al <sub>2</sub> O <sub>3</sub>	12.3	13.0	0.19	12.9	0.45	13.4	0.37
FeO <sup>T</sup>	0.72	0.53	0.34	0.32	0.20	0.69	0.27
MnO	0.03	0.02	0.04	0.01	0.02	0.06	0.17
MgO	0.04	0.02	0.02	0.01	0.03	0.03	0.04
CaO	0.46	0.41	0.04	1.44	0.24	0.45	0.13
Na <sub>2</sub> O	3.64	3.68	0.48	5.35	1.05	3.62	0.62
K <sub>2</sub> O	4.6	4.95	0.13	0.43	0.06	4.72	0.17
P <sub>2</sub> O <sub>5</sub>	<0.01	0.02	0.03	0.02	0.03	0.02	0.03
LOI	0.42				0.00		
Total	98.5	100.0	0.73	99.8	0.88	99.5	1.79
H <sub>2</sub> O <sup>e</sup>	0.12 ± .05						
Point counts <sup>f</sup>	vol%						
Qtz	0.35						
San	1.04						
Plag	0.48						
Bte	0.36						
Ox	0.03						
Gdms	97.7						

<sup>a</sup> Geochemical analyses of the whole rock by ICPMS (see text)

<sup>b</sup> Average microprobe analyses of the groundmass glass

<sup>c</sup> Average microprobe analyses of glasses immediately adjacent to sanidine crystals (see text)

<sup>d</sup> Starting composition used in the phase equilibrium and decompression experiments

<sup>e</sup> Average water content of groundmass glass measured using FTIR spectrometry (see text)

<sup>f</sup> Mineral abbreviations: *qtz* quartz, *san* sanidine, *plg* plagioclase, *bte* biotite, *ox* oxides, *gdms* groundmass. Apatite, zircon and allanite were also identified as accessory mineral phases in SEM analysis of the natural sample

## Methods

### Sample selection

The sample selected for this study (GM-11) was collected from an outcrop of obsidian on the north side of Glass Mountain (Table 1; Fig. DR-1). The sample is selected for the presence of mineral phases (rather than aphyric), which were identified in hand sample.

### Natural sample

The obsidian GM-11 was crushed in a steel jaw crusher, then powdered in a porcelain shatter box and analyzed using LA-ICPMS for a suite of major elements at Activation Laboratories, Ltd., in Ancaster, Ontario. Chips of the natural sample were prepared as thin sections and mounted in one-inch epoxy molds and polished for electron beam analyses. A point count (consisting of 1000 points) was

conducted on a thin section to determine modal abundances. In addition, a doubly polished wafer was prepared for analysis of H<sub>2</sub>O contents in groundmass glasses, using a Nicolet 6700 Fourier transform infrared (FTIR) spectrometer with continuum microscope at the Department of Mineral Sciences, National Museum of Natural History (NMNH), in Washington, DC.

### Phase equilibrium experiments

#### Starting material

Pieces of obsidian GM-11 were crushed to a fine powder using an agate mortar and pestle. An aliquot (~10 g) of this powder was placed in a platinum crucible, heated to 1450 °C in air, held for six hours, quenched to a glass. The glass was inspected for the presence of crystals, was determined to be aphyric and was then repowdered and used as the experimental starting material (Table 1). This

**Table 2** Experimental conditions and run products

#	T (°C)	P (MPa)	P <sub>f</sub> (MPa)	Duration (h)	Run products
Phase equilibrium experiments					
G29	700	225	–	72	gl, bte, tmt
G10	700	200	–	48	gl, san, qtz, bte, tmt
G28	700	200	–	72	gl, san, qtz, bte, tmt
G17	700	160	–	72	gl, san, qtz, bte, tmt
G19	700	130	–	72	gl, san, qtz, bte, tmt
G27	700	100	–	120	gl, san, qtz, plg, bte, tmt
G25	700	80	–	120	san, qtz, plg, il, al, tmt, cpx
G31	725	200	–	72	gl, bte, tmt
G32	725	175	–	120	gl, bte, tmt
G20	725	150	–	72	gl, bte, tmt
G30	725	125	–	72	gl, san, qtz, bte, tmt
G21	725	100	–	72	gl, san, qtz, plg, cpx, tmt
G26	725	80	–	120	gl, san, qtz, plg, cpx, tmt
G11	750	200	–	72	gl, bte, tmt
G29	750	125	–	48	gl, bte, tmt
G28	750	100	–	72	gl, san, qtz, cpx, tmt
G2	775	225	–	75	gl, bte
G16	800	175	–	72	gl, bte
G14	800	150	–	72	gl, bte, tmt
G24	810	75	–	120	gl, san, qtz, tmt
G12	825	125	–	48	gl, tmt
G15	850	100	–	72	gl, tmt
Decompression experiment					
G41	700	225	100	216	gl, san, qtz, plg, bte, tmt

Phase equilibrium experiments are held at a constant pressure (noted as P). For the decompression experiment, P notes the initial pressure and P<sub>f</sub> notes the final pressure. Abbreviations: *gl* glass, *bte* biotite, *tmt* titanomagnetite, *san* sanidine, *qtz* quartz, *plg* plagioclase, *cpx* clinopyroxene, *il* ilmenite, *al* allanite. All runs are H<sub>2</sub>O saturated. Because the 100 % crystallinity was achieved in 120 h for the experiment that marks the solidus (i.e., 700 °C, 80 MPa), we presume that our run durations are sufficient enough so that near-equilibrium conditions are achieved

experimental design allowed us to create a starting material for phase equilibrium experiments that was completely free of pre-existing crystals and nuclei.

#### Experimental apparatus, conditions and strategy

Experiments were conducted in cold-seal Waspaloy (nickel alloy) pressure vessels at the National Museum of Natural History (NMNH) in Washington, DC. Water

was the pressurizing medium, and experimental pressures and temperatures ranged from 75 to 250 MPa and 700 to 850 °C (Table 2). For each experiment, 10–30 mg of starting material was placed inside 3-mm OD gold tubing, to which ~10 % of the sample weight in DI water was added to ensure that all runs would be saturated with 100 % H<sub>2</sub>O fluid. Gold capsules were sealed using a PUK-3 welding system. Experiments were brought up to their final temperature and pressure over a two-hour period, with care taken not to overshoot the desired run conditions. The objective was to avoid nucleation and growth of mineral phases at conditions other than the target run conditions. Experiments were held at their final conditions for periods ranging from 48 to 120 h (Table 2). In general, the experiments conducted at the lowest temperatures and pressures (i.e., highest melt viscosities) correspond to the longest durations (e.g., experiment G25 equilibrated at 700 °C and 80 MPa was held for 120 h; Table 2). During quenching, the temperature in the hot spot of the pressure vessel (~1 inch in length) was cooled to <500 °C (~the glass transition temperature) in <30 s by blowing compressed air on the charge, then plunging the vessel into a cold water bath (see Waters et al. 2015 for more details).

The system of Waspaloy pressure vessels and nickel-filler rods used in the phase equilibrium experiments has an intrinsic oxygen fugacity ( $fO_2$ ) of  $\Delta NNO + 1 \pm 0.5$  (Geschwind and Rutherford 1995). Venezky and Rutherford (1999) show that the  $fO_2$  imposed by the Waspaloy pressure vessels and nickel-filler rods may vary significantly and is dependent on the age and degree of oxidation of the nickel-filler rod. Because  $fO_2$  is only broadly constrained in these experimental vessels, experiments are used to determine the plagioclase- and sanidine-liquid equilibria, whereas Fe-bearing mineral stability curves (e.g., biotite) are reported but not used.

#### Isothermal decompression experiment

##### Starting material

The starting material and capsule design used in decompression experiments were identical to those used in the phase equilibrium experiments.

##### Strategy, experimental apparatus and conditions

Comparison of the natural sample to phase equilibrium experiments in the following sections highlights the potential importance of superheating (a purge of nucleation sites) followed by slow decompression to form the Glass Mountain obsidians (discussed below) in the formation of the phenocryst assemblage. The decompression experiment that would most accurately test the effect of an absence of nucleation sites on crystallization in obsidians should

be initiated from superliquidus conditions and continuously decompressed to the final pressure. However, such an experiment was challenging to achieve due to the range of pressures that must be traversed and the method by which continuous decompression rates are achieved in our apparatus. The experimental apparatus consists of four Waspaloy pressure vessels and furnaces connected to a single pressure line. During a decompression, three of the four pressure vessels are cooled at a controlled rate to generate a constant decrease in pressure in the fourth pressure vessel, which is held at a constant temperature and contains the experimental charge. The magnitude of the pressure drop required for a decompression experiment to initiate from above-liquidus conditions to the final below-liquidus conditions is 125 MPa, which is too large an interval to traverse without a ~90-min pause to reheat the three vessels acting as pressure actuators.

As a result, we chose to conduct a single-step decompression from superliquidus conditions to a final pressure to examine how crystallization may proceed in this melt starting from nuclei-free conditions. For the single-step decompression, the experiment was taken to and held at an initial temperature and pressure of 700 °C and 225 MPa( $P_{H_2O}$ ), respectively, for four hours, which should be more than sufficient time to purge the system of nucleation sites, based on kinetic experiments by Vetere et al. (2013). The initial condition corresponds to a position above the sanidine-in curve and was selected so that the melt is both hydrated and contains no nucleation sites or pre-existing crystals at the initiation of decompression. After four hours, the experiment was rapidly ( $>100$  MPa/s), isothermally (700 °C) decompressed to a final condition, 100 MPa( $P_{H_2O}$ ), which corresponds to a position below both the plagioclase- and sanidine-in curves. While the rate used to reduce pressure in the single-step decompression is uncharacteristic of effusively erupted obsidians (e.g.,  $\leq 2$  MPa/h; Castro and Gardner 2008), rapid decompression was required to ensure that no nucleation sites form. The decompression was held for a duration of nine days, corresponding to an integrated decompression rate of 0.56 MPa/h, which is consistent with other proposed eruptive rates for obsidians (Castro and Gardner 2008; Waters et al. 2015). The duration was selected to ensure that some crystallization would occur in this liquid, considering any potential barriers associated with potentially prolonged nucleation delays or sluggish diffusion of elements to the crystal interface due to elevated melt viscosities.

## Analytical methods

### Natural sample

High-resolution images and high-definition energy-dispersive X-ray spectrometry (EDX) element maps of sanidine

phenocrysts in the natural sample were collected using the FEI Nova NanoSEM 600 (scanning electron microscope) at the NMNH, Department of Mineral Sciences, to establish the diversity of textures and range of compositions within the natural obsidian sample. Map areas were adjusted so that sanidines composed the greatest proportion of the map area, and thus, areas varied as a function of the size of individual crystals. In all cases, the maps were collected at a resolution of approximately 1 pixel/ $\mu\text{m}^2$ . Spectra were collected for nine major elements (Si, Ti, Al, Fe, Mg, Ca, Na, K and O), and a separate file of grayscale values (based on BSE) was collected using the Noran System Six and a Si-drift detector. The spectral arrays were combined and processed with MATLAB to create a map of mol% orthoclase ( $X_{Or}/X_{Or} + X_{Ab} * 100$ ) content in the sanidine crystals. The Si, Al, Ca, Na, K and O maps were used to calculate proportions of anorthite, albite and orthoclase, to derive the mol% Or corresponding to each pixel. Pixels corresponding to areas of groundmass and epoxy were filtered out using counts of Si, K and Fe and the co-registered backscatter electron image, so that final maps only consist of pixels with values of orthoclase compositions for the investigated sanidines.

Results of SEM mapping of sanidines were confirmed by electron microprobe analyses using the JEOL 8900 Superprobe at the NMNH, Department of Mineral Sciences. An accelerating voltage of 15 kV and beam current of 10 nA with a point beam ( $<1$   $\mu\text{m}$ ) were used for sanidine analyses. The accuracy of the sanidine microprobe analytical method was assessed by periodically measuring Smithsonian standards, Amelia Albite, Kakanui Anorthoclase, and Great Sitkin Anorthite, throughout the run duration. In all cases, the average values obtained for secondary standards match reported values well within  $2\sigma$  (Data Repository Table DR-1). The compositions of sanidine determined by microprobe analysis and SEM mapping are in good agreement (Fig. DR-2). Analyses of groundmass glasses were collected with the JEOL 8900 Superprobe, using a defocused beam (5  $\mu\text{m}$ ), a beam current of 5 nA and count times for each element ranging between 20 and 30 s. Na in glasses was measured using the Time-0 intercept function in the Probe for Windows software with on-peak counting for 30 s with three subcounting intervals of 10 s to assess and correct for Na loss. The accuracy of the microprobe analytical method for glasses was assessed by periodically measuring Smithsonian Yellowstone glass standard, VG-568, through the run duration. The average values obtained for the secondary standard match the certified standard values well within  $2\sigma$  (Data Repository Table DR-1).

The  $H_2O$  contents of groundmass glasses were measured in a doubly polished wafer of obsidian GM-11. As a result of low water contents, the only routinely



identifiable absorption band was the molecular water ( $\text{H}_2\text{O}$ ) peak at  $3570\text{ cm}^{-1}$ . Spectral peak heights were converted to total water contents using a molar absorptivity of  $80\text{ L mol}^{-1}\text{ cm}^{-1}$  (Leschik et al. 2004; Liu et al. 2005).

#### *Phase equilibrium experiments*

The charges quenched from the phase equilibrium experiments were peeled open, chips of the run products were removed, then mounted in epoxy and polished for microprobe analyses. Glasses and minerals in the run products were also analyzed with the JEOL 8900 Superprobe at the NMNH, Department of Mineral Sciences, following the methods described above. Once the melt compositions were determined,  $\text{H}_2\text{O}$  contents were calculated using the  $\text{H}_2\text{O}$  solubility model of Zhang et al. (2007), which has been independently demonstrated to accurately record water contents for rhyolites (e.g., Waters et al. 2015).

Modal abundances of mineral phases in the equilibrium experiments that crystallized sanidine and quartz were calculated using BSE images of experimental run products and an image analysis software, GraphClick, which determines the area composed by each mineral phase based on grayscale images. Image analysis of the run products is favored over linear regression analysis, due to the similarity between the glass compositions and the average mineral compositions.

#### *Decompression experiment*

The charge from the decompression experiment was peeled open, and the run product was removed, mounted in epoxy and polished for SEM imaging using the FEI Nova NanoSEM 600 at the NMNH, Department of Mineral Sciences.

## Results

### Natural sample

#### *Petrography*

The composition of the natural sample is presented in Table 1, along with the modal abundances determined by point count. Mineral phases identified in the natural sample include sanidine + quartz + plagioclase + biotite + oxides + apatite + zircon + allanite (Table 1). Obsidian sample GM-11 consists mostly of glass (97.7 %) with <2.3 % crystals (Table 1; Fig. DR-3). Sanidine is the most abundant mineral phase, followed by plagioclase, quartz and then opaque minerals. Apatite, zircon and allanite are infrequently observed using electron beam techniques, occur in

too low abundance to be routinely identified during point counts and are tabulated as trace mineral phases.

#### *Sanidine in the natural sample: sizes, textures and composition*

Sanidines are typically  $\leq 300\text{ }\mu\text{m}$  and exhibit granophyric textures (Fig. 1), characterized by intergrowths of quartz incorporated into their lattices. Individual sanidines span a range of compositions, typically from  $\text{Or}_{78}$  to  $\sim\text{Or}_{40}$  (Fig. 1). Sanidines are normally zoned, where the most potassic compositions are found in the interiors and compositions are progressively more sodic toward the margins (Fig. 1). Sanidine crystals also feature small ( $\leq 10\text{ }\mu\text{m}$ ) faceted regions that have anorthositic compositions (Fig. 1), which are interpreted to be a separate mineral phase (plagioclase). Sanidines are always mantled by a melt boundary layer that is depleted in  $\text{K}_2\text{O}$  and enriched in  $\text{CaO}$ , relative to the groundmass glass (Table 1; Fig. 1). In summary, sanidines in the natural sample have four distinct characteristics: They (1) occur as sparse, small ( $<300\text{ }\mu\text{m}$ ) crystals, (2) exhibit granophyric textures, (3) span a wide range in composition reflecting normal zoning and are (4) mantled by a boundary layer of depleted melt. The obsidian contains minor amounts of water (0.12 wt%; Table 1) as determined by FTIR, indicative of significant degassing to conditions of  $\sim 1$  bar (surface).

### Phase equilibrium experiments

Mineral phases that crystallized in the phase equilibrium experiments are sanidine, quartz, plagioclase, biotite, titanomagnetite, ilmenite, allanite, apatite and zircon (Table 2; Fig. 2). Biotite is the low-temperature liquidus phase, and titanomagnetite is the high-temperature liquidus phase for GM-11 (Fig. 2). Sanidine and quartz co-saturate at temperatures and  $P_{\text{H}_2\text{O}}$  values higher than those corresponding to the plagioclase-in curve. Ilmenite and allanite saturate at the solidus (the lowest temperatures and  $P_{\text{H}_2\text{O}}$  values). Apatite and zircon are observed in many experiments as a trace phase; however, due to their sparse abundance, specific mineral-in curves were not defined.

#### *Mineral abundances*

The amount of glass (as vol%) in the run products (Fig. 2, shown below each experiment that crystallized sanidine and quartz) decreases dramatically as the solidus is approached. BSE images of the run products of the experiments conducted at  $700\text{ }^\circ\text{C}$  illustrate the increase in crystallinity as  $P_{\text{H}_2\text{O}}$  decreases from 160 to 80 MPa (5.5–4 wt%  $\text{H}_2\text{O}$ ; Figs. 2, 3). A decrease in 80 MPa (at  $700\text{ }^\circ\text{C}$ ) corresponds to a decrease in melt  $\text{H}_2\text{O}$  content of 1.5 wt% (using

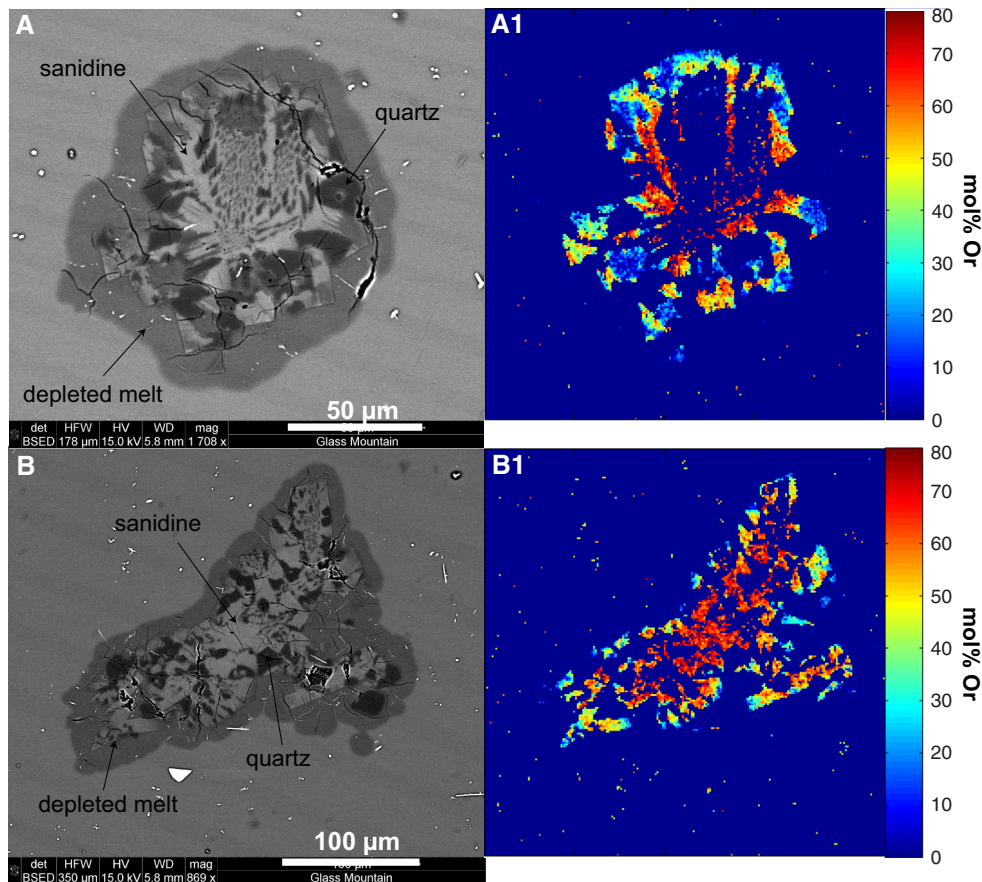


**Fig. 1** BSE images of two sanidine crystals representative of those in GM-11 are shown in A and B and feature a granophyric texture (intergrowths of quartz in sanidine) and the boundary layer of melt depleted in  $K_2O$  (see text). Maps of mol% Or measured in the crys-

tals of sanidine (A&B) using EDX mapping are shown next to the BSE images and are noted as A1 (corresponding to the orthoclase map of the crystal shown in A) and B1 (corresponding to the orthoclase map of the crystal shown in B)

the solubility model of Zhang et al. 2007) and results in an increase in crystallinity from <10 to 100 % (Fig. 2; Table 2). Similarly, at a constant pressure of 80 MPa, an increase in temperature of 100 °C (from 700 to 800 °C) shifts the melt from subsolidus to conditions where only titanomagnetite is stable (Fig. 2).

#### Crystal sizes and textures

In all phase equilibrium experiments, mineral phases occur as small crystals ( $\leq 30 \mu\text{m}$ ) (Fig. 3). At conditions near the sanidine + quartz-in curve, sanidines occur as sparse laths ( $\leq 10 \mu\text{m}$ ) and increase in size to  $\leq 30 \mu\text{m}$  at conditions near the solidus. Quartz occurs as small ( $\leq 5 \mu\text{m}$ ), sparse, faceted individual grains in phase equilibrium experiments near the sanidine + quartz-in curve and gradually increases in size ( $\leq 15 \mu\text{m}$ ) as the solidus is approached. Plagioclase mostly grows on sanidine crystals and never reaches sizes  $>15 \mu\text{m}$ .

#### Melt and crystal compositions

Compositions of experimental glasses and sanidines are shown in Table 3 for those experiments beneath the sanidine + quartz-in curve. All analyzed compositions of glass and sanidine are reported in the Data Repository (Table DR-2A&B). Melt compositions do not change dramatically as the solidus is approached (i.e., experiments run at 700 °C; Table 3), despite the dramatically increasing degree of crystallization in the experimental run products. Sanidine compositions (shown above each experiment in Fig. 2) span a range of compositions from  $Or_{75}$  to  $Or_{51}$ , over a range of temperatures (700–725 °C) and pressures [200–80 MPa( $P_{H_2O}$ )] and corresponding water contents (6.6–4.3 wt%  $H_2O$ ) (Fig. 2; Table 3). Sanidine compositions are enriched in the orthoclase component in experiments conducted at higher  $P_{H_2O}$  (i.e., experiment G10 with 6.6 wt%  $H_2O$  has sanidine with the highest measured  $Or_{75}$ ) at a given temperature. Similarly, at a constant  $P_{H_2O}$ ,

**Fig. 2** Phase equilibrium experiment results are summarized with a diagram. Also shown are isopleths of dissolved melt  $H_2O$  (as large-dashed lines) calculated using Zhang et al. (2007) and isopleths of melt viscosity calculated using Hui and Zhang (2007). Mineral phases grown in each experiments are coded in a six-panel rectangle keyed in the figure with the abbreviations as follows: *q* quartz, *p* plagioclase, *s* sanidine, *b* biotite, *t* titanomagnetite, *c* clinopyroxene. A phase is indicated as present, if a square is black. For the experiments that crystallized sanidine, compositions of sanidine, as  $X_{Or}$ , are shown above each experiment, and the proportion of glass in each experiment is shown below each experiment

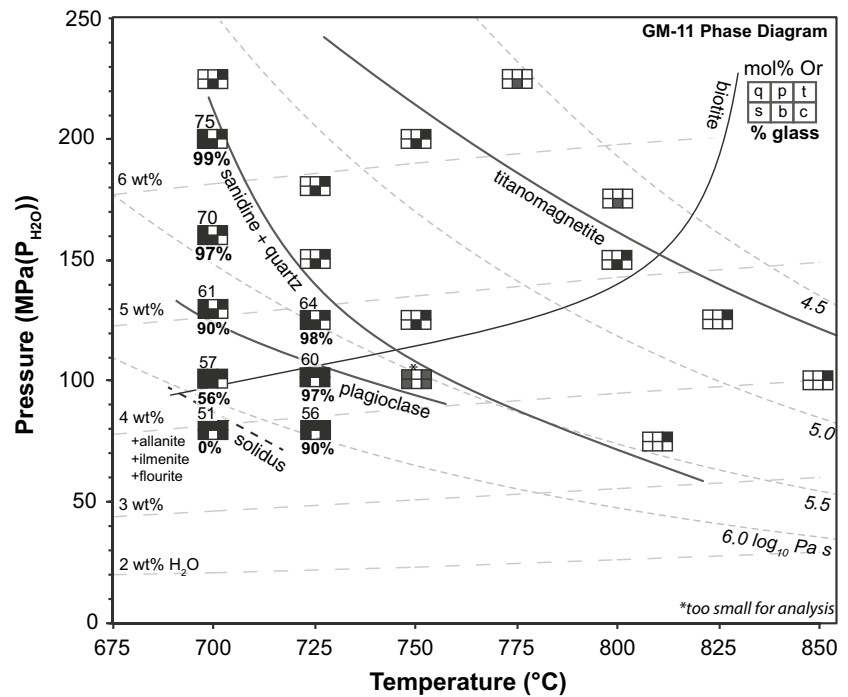


**Fig. 3** Representative BSE images of phase equilibrium experiments conducted at 700 °C are shown for pressures of 160, 130, 100 and 80 MPa. Sanidine (bright laths) and quartz (small, dark, gray rounded crystals) dominate the phase assemblage and increase dramatically in abundance as the solidus (d, 700 °C, 80 MPa) is approached. Plagioclase appears close to the solidus and is a darker gray relative to sanidine

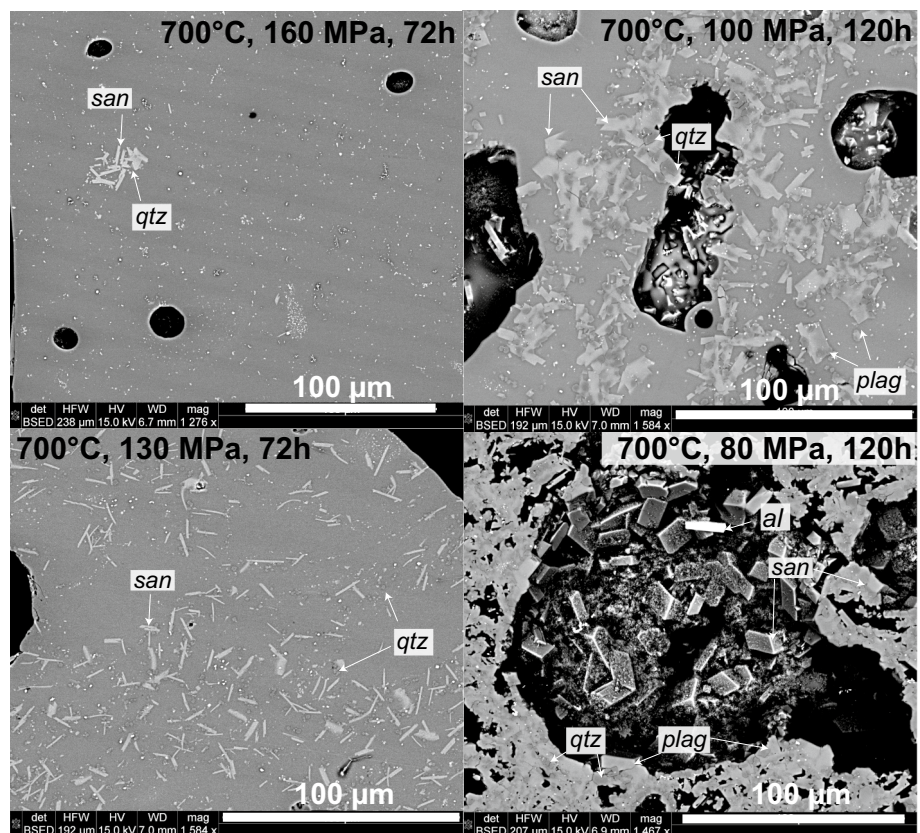




**Table 3** Compositions of sanidines and glasses

#	T	<sup>39</sup> P <sub>i</sub>	<sup>40</sup> P <sub>f</sub>	Phase	% <sup>c</sup>	n	SiO <sub>2</sub>	TiO <sub>2</sub>	Al <sub>2</sub> O <sub>3</sub>	FeO	MnO	MgO	CaO	Na <sub>2</sub> O	K <sub>2</sub> O	P <sub>2</sub> O <sub>5</sub>	Total	wt% H <sub>2</sub> O <sup>d</sup>	X <sub>An</sub>	X <sub>Ab</sub>	X <sub>Or</sub>
Phase equilibrium experiments																					
G10	700	200	-	Gl	99	12	76.9	0.06	13.8	0.63	0.07	0.04	0.50	3.32	4.73	0.02	92.9	6.15			
				Iσ			0.52	0.03	0.26	0.20	0.05	0.03	0.06	0.41	0.11	0.01	1.10	0.04			
				San	1	1	65.8		18.2	0.56			0.28	2.63	12.5		100.0		1.4	23.8	74.8
G17	700	160	-	Gl	92	8	77.0	0.06	13.9	0.48	0.06	0.02	0.50	3.44	4.59	0.02	93.3	5.50			
				Iσ			0.51	0.05	0.38	0.18	0.07	0.02	0.08	0.27	0.14	0.02	1.25	0.03			
				San	7	10	66.2		18.1	1.19	0.03	0.23	0.35	2.75	10.4		99.2		1.97	28.1	69.9
				Iσ			0.96		0.64	0.49	0.02	0.11	0.06	0.22	0.61		0.91		0.43	1.31	1.27
G19	700	130	-	Gl	85	15	77.7	0.09	13.4	0.59	0.03	0.02	0.50	3.38	4.28	0.01	94.6	4.97			
				Iσ			0.90	0.04	0.41	0.16	0.05	0.02	0.08	0.75	0.07	0.02	0.56	0.05			
				San	12	11	68.2		17.6	0.39	0.02	0.03	0.36	3.65	9.20		99.4		2.00	36.9	61.1
				Iσ			1.33		0.81	0.36	0.02	0.05	0.13	0.31	0.75		1.21		0.72	2.26	2.75
G27	700	100	-	Gl	63	6	77.7	0.06	13.3	0.61	0.06	0.01	0.50	3.56	4.36	0.02	93.2	4.35			
				Iσ			0.39	0.03	0.17	0.19	0.04	0.02	0.08	0.24	0.17	0.03	0.65	0.04			
				San	20	7	67.2		18.6	0.19	0.02	0.00	0.35	4.51	9.32		100.2		1.8	41.6	56.6
				Iσ			0.56		0.14	0.10	0.02	0.00	0.08	0.25	0.28		0.25		0.37	0.97	0.85
G25	700	80	-	San	<1	4	65.5		19.4	0.13	0.03	0.00	0.33	3.84	10.8		100.0		2.1	46.5	51.4
				Iσ			0.51		0.69	0.07	0.03	0.00	0.08	0.19	0.17		0.65		0.39	0.91	1.03
G30	725	125	-	Gl	98	9	76.5	0.07	13.5	0.75	0.08	0.02	0.47	3.88	4.70	0.01	93.7	4.83			
				Iσ			0.6	0.03	0.42	0.22	0.08	0.02	0.08	0.55	0.12	0.02	0.59	0.04			
				San			65.5		19.4	0.13	0.03	0.00	0.33	3.84	10.8		100.0		1.6	34.5	63.8
				Iσ			0.40		0.29	0.07	0.07	0.02	0.04	0.37	0.15	0.03	1.19	0.02	0.39	0.91	1.03
G21	725	100	-	Gl	97	7	76.6	0.05	13.8	0.73	0.07	0.04	0.49	3.65	4.64	0.02	94.8	4.29			
				Iσ			0.40	0.04	0.29	0.07	0.07	0.02	0.04	0.37	0.15	0.03	1.19	0.02	2.37	37.5	60.1
				San	1	7	67.1		19.1	0.28	0.01	0.01	0.44	3.85	9.39		100.1		0.11	1.51	1.49
				Iσ			0.58		0.72	0.13	0.02	0.03	0.02	0.17	0.44		0.41				
G26	725	80	-	Gl	90	8	76.5	0.08	13.8	0.60	0.04	0.04	0.46	3.92	4.60	0.01	94.3	3.84			
				Iσ			0.46	0.05	0.37	0.17	0.04	0.04	0.10	0.37	0.17	0.02	0.41	0.02			
				San	8	5	66.1	0.03	18.7	0.30	0.01	0.07	0.37	4.37	8.77		98.7		1.97	42.2	55.9
				Iσ			0.38	0.04	0.23	0.26	0.03	0.08	0.09	0.42	0.21		0.55		0.45	2.35	2.52
Decompression experiment <sup>e</sup>																					
G41	700	225	100	Gl	64	8	77.0	0.05	13.5	0.57	0.12	0.02	0.47	3.85	4.39	0.01	93.8	4.38			
				Iσ			0.66	0.03	0.29	0.29	0.10	0.02	0.08	0.22	0.10	0.01	0.68	0.01			

<sup>a</sup> Initial pressure: In the case of the phase equilibrium experiments, initial pressure corresponds to run pressure. In the decompression experiment, initial pressure corresponds to the initial annealing conditions of the experiment

<sup>b</sup> Final experimental pressure (only applies to the decompression experiment)

<sup>c</sup> A bunnances determined for those samples that crystallized sanidine (see text for detail)

<sup>d</sup> Water contents calculated using melt compositions and the solubility model of Zhang et al. (2007)

<sup>e</sup> Because the decompression experiment was only conducted in an attempt to recreate a crystal texture (see text), sanidine compositions were not collected

sanidine compositions are enriched in the orthoclase component at hotter temperatures.

### Decompression experiment

Sanidine, plagioclase, quartz and titanomagnetite were the major phases grown in the decompression experiment (Fig. 4). The experiment achieved a degree of crystallization closely approximating the equilibrium degree of crystallinity corresponding to 700 °C and 100 MPa (Table 3) in the nine day experimental duration. Unlike the equivalent phase equilibrium experiment (Fig. 3), sanidine crystals range in size from 30 to  $\geq 80$   $\mu\text{m}$  and exhibit granophyric textures (intergrowths of quartz in the sanidine lattice; Fig. 4). Quartz crystals range in size from 15 to  $\geq 30$   $\mu\text{m}$ . Plagioclase crystals preferentially grow on pre-existing sanidine grains.

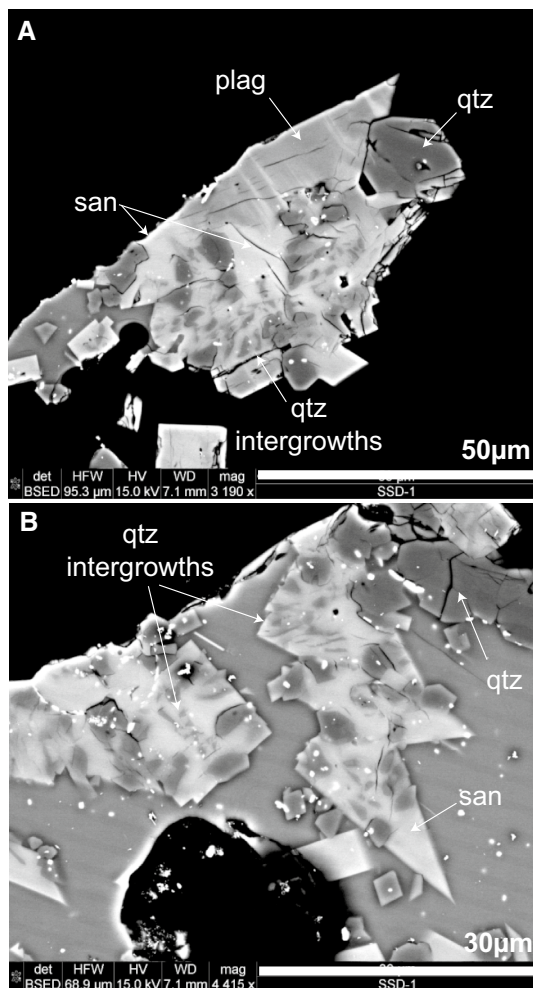


**Fig. 4** Image A and B are examples of granophyric textures representative of those grown in the single-step decompression experiment

## Discussion

### Comparison of the natural sample to the phase equilibrium experiments

All mineral phases observed in the natural obsidian, GM-11, are found to be stable over a range of conditions in the phase equilibrium experiments, and, therefore, all natural crystals could have plausibly grown from the melt and are interpreted to be phenocrysts. The four most abundant phenocryst phases in GM-11 are sanidine, quartz, plagioclase and biotite, and the phase equilibrium experiments demonstrate that these mineral phases co-exist at conditions near the solidus (Fig. 1). It would be problematic, however, to interpret these conditions as storage conditions for GM-11 for two reasons. First, the experiments in this region of the phase diagram often contain  $\gg 10$  % crystals, which contrasts dramatically with the low degree of crystallinity in the sample (2.3 vol%; Table 1). Moreover, experiment G27, conducted at 700 °C and 100 MPa (Fig. 2; Table 2), achieved 44 % crystallization in 120 h, which suggests that crystallization is not significantly inhibited at steady-state (storage) conditions, despite the high melt viscosity ( $>5.5 \log_{10}$  Pa-s; Fig. 2). Secondly, sanidine in the natural sample spans a range of composition ( $\text{Or}_{78-40}$ ; Fig. 1), whereas sanidine grown in the region of the phase diagram where quartz, sanidine and plagioclase co-saturate [e.g.,  $\leq 725$  °C and  $< 130$  MPa( $P_{\text{H}_2\text{O}}$ )] spans a limited range of compositions ( $\text{Or}_{51-60}$ ; Fig. 2).

The apparent discrepancy between the abundance and compositions of crystals in the run products of equilibrium experiments and those in the natural sample can be resolved if crystallization is induced by a dynamic process. Cooling (e.g., Iezzi et al. 2011; Vetere et al. 2013) and degassing (e.g., Hammer and Rutherford 2002; Couch et al. 2003; Castro and Gardner 2008; Waters et al. 2015) are two mechanisms which have been experimentally demonstrated to inhibit crystallization due to kinetic effects on nucleation and growth rates. During these dynamic processes, crystal compositions reflect changing intensive parameters (e.g., temperature) and/or melt compositions (e.g., dissolved melt  $\text{H}_2\text{O}$ ). A precedent exists for this hypothesis in the literature, as recent work by Mollo et al. (2015) uses sanidine as the basis for a hygrometer/thermometer for alkaline liquids, indicating that changes in  $f_{\text{H}_2\text{O}}$  and temperature will change the sanidine composition in equilibrium with a liquid composition. Application of the hygrometer of Mollo et al. (2015) to sanidine in the Glass Mountain obsidian requires an extrapolation of the model to aluminous liquid compositions, and as a result, the water contents derived from that model are over-predictions. The conditions under which

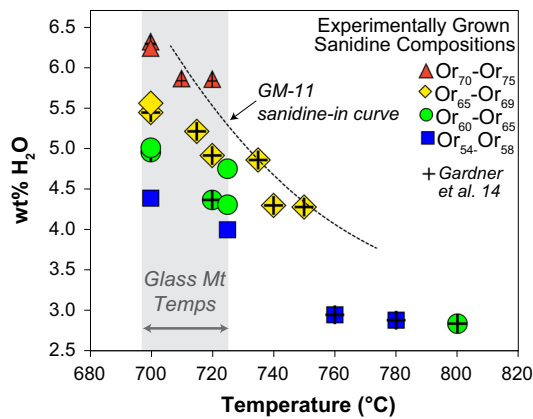


**Fig. 5** Sanidine compositions grown in the phase equilibrium experiments (Table 3) are plotted as a function of their experimental temperatures and water contents, along with sanidine compositions from Gardner et al. (2014) (marked with a cross). Sanidine compositions increase in  $X_{Or}$  with both increasing  $H_2O$  contents and increasing temperatures. Also shown as a grey box are the pre-eruptive temperatures obtained from the Glass Mountain lavas (see text for discussion)

crystallization of the Glass Mountain obsidians occurred, and therefore the mechanism driving crystallization, may be determined by comparison of sanidine compositions in the natural sample with compositions grown in the phase equilibrium experiments from this study.

#### Sanidine composition: effects of temperature and $P_{H_2O}$

A comparison of the range of sanidine compositions in the natural sample ( $Or_{78-40}$ ; Fig. 1) with the range of compositions grown in experiments ( $Or_{75-51}$ ; Fig. 2) demonstrates that all of the sanidine compositions could have plausibly grown from the liquid and all compositions are interpreted to be phenocrystic. At 700 °C and 200 MPa( $P_{H_2O}$ ), the sanidine composition in equilibrium with the melt and 6.2 wt%  $H_2O$  (calculated using Zhang et al. 2007; Fig. 3) is  $Or_{75}$ , which closely matches the most orthoclase-rich sanidine ( $Or_{78}$ ) observed in the natural sample. In phase equilibrium experiments conducted at pressures <200 MPa( $P_{H_2O}$ ) and 700 °C, the equilibrium sanidine composition is increasingly more sodic as  $P_{H_2O}$  (i.e., melt  $H_2O$  content) decreases. Equilibrium sanidine compositions are generally more sodic with decreasing temperature, at a constant  $P_{H_2O}$  value (Fig. 2). Therefore, either gradual degassing of  $H_2O$  and/or cooling could plausibly explain the range of sanidine compositions observed in the natural sample.

The magnitude of the individual effects of temperature and dissolved melt  $H_2O$  on sanidine composition is evaluated in Fig. 5 using  $H_2O$ -saturated phase equilibrium experiments from Fig. 2 and  $H_2O$ -saturated experiments conducted on the Bishop Tuff by Gardner et al. (2014) over a range of temperatures (700–800 °C), pressures

(50–200 MPa) and  $H_2O$  contents (2.8–6.3 wt%). At constant  $H_2O$  content (e.g., 4.5 wt%), a decrease in temperature of ~35 °C corresponds to a decrease in ~5 mol% Or in sanidine (e.g., ~ $Or_{70}$  to  $Or_{65}$ ). At constant temperature (e.g., 700 °C), the effect of degassing ~2 wt%  $H_2O$  from the melt (e.g., ~6.5 to ~4.5 wt%) is to decrease the  $X_{Or}$  in sanidine by nearly 20 mol% (i.e., from ~ $Or_{75}$  to  $Or_{53}$ ). Both decreasing temperatures and decreasing  $H_2O$  contents have a similar effect on sanidine composition, which is to stabilize a sodium-rich sanidine (Fig. 5).

To determine which mechanism (degassing or cooling) is more likely to generate the range of sanidine compositions in GM-11, the sanidine-in curve (from Fig. 1) is shown in Fig. 5. Also shown in Fig. 5 (as a grey box) are the pre-eruptive temperatures (698–725 °C) of the Glass Mountain lavas, which are recalculated by incorporating the compositions of titanomagnetite and ilmenite pairs reported by Metz and Mahood (1991) into the geothermometer of Ghiorso and Evans (2008). In Fig. 5, the hottest pre-eruptive temperature recorded by the Glass Mountain lava (725 °C) intersects the GM-11 sanidine-in curve at ~5.3 wt%  $H_2O$ , where the equilibrium sanidine composition falls in the range of 69–65 mol% Or. Cooling from this position will only result in the crystallization of increasingly more sodic sanidine compositions, and the most potassic sanidine compositions observed in the natural sample ( $Or_{70-78}$ ) will not be grown. The total variation in pre-eruptive temperatures of lavas from Glass Mountain is 27 °C, and this range of temperature can only shift the equilibrium sanidine composition by 5–10 mol% Or, meaning that cooling alone is not sufficient enough to produce the observed range in sanidine composition in the natural sample. Alternatively, gradual degassing of >2 wt%  $H_2O$  (from ~6 to <4 wt%  $H_2O$ ) will cause the equilibrium sanidine composition to shift from 75 to <54 mol% Or. Given the limited range in pre-eruptive temperatures, it appears that changing melt  $H_2O$  contents potentially have a greater effect on shifting the equilibrium sanidine compositions than changing temperatures for GM-11. Based on the normal zoning within individual sanidine crystals (Fig. 2) and the trend in sanidine composition with dissolved  $H_2O$  (Fig. 5), we hypothesize that crystallization of sanidine in GM-11 is driven dominantly by degassing, accompanied by some degree of cooling, as it cannot be ruled out.

Comparison of the range of sanidine compositions from the natural sample with those grown in the phase equilibrium experiments suggests that crystallization of sanidine is plausibly driven by progressive degassing of 6.2 to <4 wt%  $H_2O$  at a pre-eruptive temperature of ~°C. There are several outstanding issues, however, that should be resolved to conclusively demonstrate that crystallization of sanidine occurs due to degassing. (1) Can degassing sufficiently restrict crystallization to <2.3 vol% within

the natural sample so that it is far less than the relatively extensive degrees of crystallization observed in the phase equilibrium experiments? (2) Can degassing result in the formation of sparse phenocrysts, as observed in the natural obsidian (GM-11)? (3) Is it possible for near-equilibrium compositions to crystallize in non-equilibrium abundances (e.g., <2.3 vol%)? (4) Can degassing account for the unique textures (i.e., granophyric sanidine and melt boundary layers) that are observed in the natural sample? To address the four outstanding questions, we use results presented in experimental studies from the literature, as well as mineral textures grown in the decompression experiment conducted in this study.

#### *Can degassing sufficiently restrict crystallization of sanidine?*

Numerous experimental studies document sanidine crystallization, but few are conducted on aluminous and meta-aluminous liquids. There are a wealth of phase equilibrium studies conducted on alkaline and per-alkaline liquids (Scaillet and MacDonald 2001; Scaillet and Macdonald 2003; Fabbrizio and Carroll 2008; Fabbrizio et al. 2009; Andújar et al. 2008; Andújar and Scaillet 2012a, b; Almeev et al. 2012; Martel et al. 2013) and two phase equilibrium studies on aluminous liquids (Gardner et al. 2014; Befus and Gardner 2016). Surprisingly, there are no studies documenting the kinetics of sanidine crystallization in natural liquids during dynamic conditions (i.e., degassing or cooling). As such, we apply robust conclusions from studies documenting crystallization kinetics of other mineral systems to predict the kinetics of sanidine crystallization during dynamic processes, such as degassing.

Here we evaluate whether degassing can hinder sanidine crystallization, by drawing from the vast body of literature investigating the effects of decompression on plagioclase crystallization. Decompression experiments have been utilized for the examination of plagioclase microlite crystallization (e.g., Geschwind and Rutherford 1995; Hammer and Rutherford 2002; Couch et al. 2003; Martel and Schmidt 2003; Castro and Gardner 2008; Brugger and Hammer 2010; Martel 2012), phenocryst growth (Waters et al. 2015) and general mapping of crystallization kinetics (e.g., Hammer and Rutherford 2002; Brugger and Hammer 2010; Mollard et al. 2012; Shea and Hammer 2013). Among the existing experimental studies, there are significant variations in experimental design from decompression style (e.g., continuous, multi-step and single-step decompression) to starting material (e.g., crystal-free glass or crushed pumice), melt composition and initial and final conditions, which makes it challenging to directly compare one study to another to draw robust conclusions about effects

of decompression on crystallization. Comparison of the experimental studies in the literature, however, does reveal that the conditions of a melt (i.e., position relative to the liquidus) prior to decompression will strongly influence the crystallization kinetics of a melt.

The importance of the starting conditions, and therefore the starting materials, for decompression experiments can be fully appreciated with a comparison of the studies of Brugger and Hammer (2010) and Waters et al. (2015), where continuous decompression experiments were conducted to determine the crystallization kinetics of plagioclase in H<sub>2</sub>O-saturated rhyolites. Brugger and Hammer (2010) found that the final pressure of the experiment exerted the strongest control on the degree of crystallization in their experiments initiated from below the plagioclase-in curve. In contrast, Waters et al. (2015) found that decompression rate exerted the strongest control over the degree of crystallization in their experiments initiated from above the liquidus. The experiments of Brugger and Hammer (2010) achieved crystallization of plagioclase at decompression rates ranging from 0.1 MPa/h to 10 MPa/h. The experiments of Waters et al. (2015) achieved crystallization of plagioclase at rates  $\leq 0.8$  MPa/h, whereas at rates  $\geq 1$  MPa/h, run products consisted of only glass (i.e., no crystal nucleation and growth occurred).

A significant difference between the two studies is that decompression of the Brugger and Hammer (2010) experiments was initiated after an annealing period at conditions below the plagioclase-in curve, allowing crystals and nucleation sites to form. The experiments of Waters et al. (2015) were decompressed following an annealing period at conditions above the plagioclase-in curve to ensure that the experiments contained no pre-existing crystals or nucleation sites. Moreover, the starting material used in the experiments of Brugger and Hammer (2010) was a crushed pumice (i.e., contained pre-existing crystals), whereas Waters et al. (2015) used a superheated rhyolite that was purged of all crystals and nuclei (i.e., pure glass). The contrast between the results of Brugger and Hammer (2010) and Waters et al. (2015) is striking as both experimental studies were conducted on rhyolites, under H<sub>2</sub>O-saturated conditions, using continuous decompression experiments, and the only significant difference is that one series began from plagioclase-saturated conditions and the other did not. This comparison underscores that one of the most important controls on crystallization kinetics of melts is the presence or absence of pre-existing nucleation sites and clearly demonstrates the only scenario where degassing-induced crystallization resulting from decompression will successfully hinder crystallization is one in which the melts begin above the liquidus (i.e., no pre-existing nucleation sites).



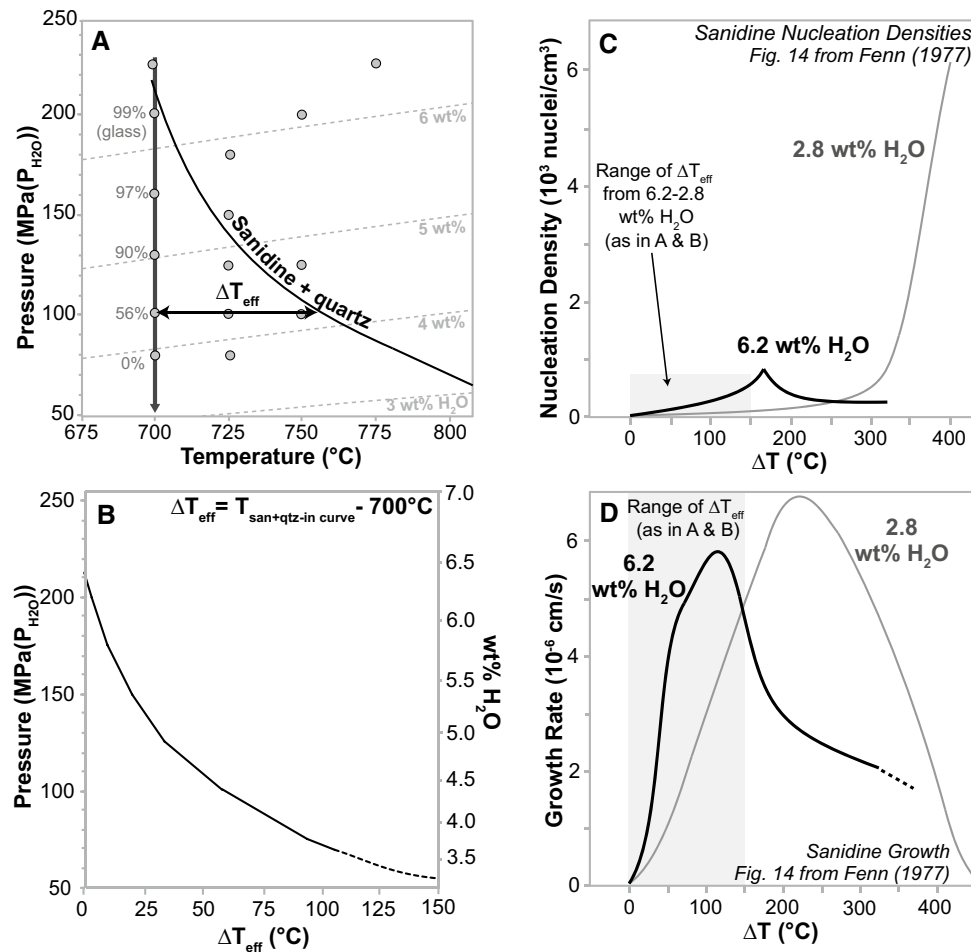


**Fig. 6** **a** The degree of effective undercooling ( $\Delta T_{\text{eff}}$ ) relative to the sanidine + quartz-in curve (from Fig. 2) is shown for a decompression pathway at 700 °C. **b** The effect of decreasing pressure (on the left axis) on the  $\Delta T_{\text{eff}}$  values is shown for the decompression pathway at 700 °C featured in A. Also shown in B are the H<sub>2</sub>O contents that corresponding to the pressures, illustrating that degassing has a similar effect on  $\Delta T_{\text{eff}}$  as decompression. **c** The sanidine nucleation densities from Fenn (1977) are shown as a function of the degree of undercooling for an experimental series conducted at 6.2 wt% H<sub>2</sub>O and another at 2.8 wt% H<sub>2</sub>O. The two curves featured in C are fitted using values of nucleation densities from many experiments conducted at a

constant water content (i.e., 6.2 or 2.8 wt%) at different values of  $\Delta T$ . Also shown in (c) is the range of  $\Delta T_{\text{eff}}$  values experience by the natural sample (from b) (as a gray box), which illustrates that nucleation densities are predicted to remain low over the range of  $\Delta T_{\text{eff}}$  values traversed by the natural sample. **d** Sanidine growth rates experimentally obtained from Fenn (1977) are shown for the experimental series conducted at 6.2 and 2.8 wt% H<sub>2</sub>O. **d** The range of  $\Delta T_{\text{eff}}$  values traversed by the natural sample (from b) is also shown as a gray box and illustrates that as degassing occurs the natural sample should remain in a region characterized by elevated growth rates

### Can degassing inhibit nucleation?

To establish whether degassing can effectively suppress extensive nucleation and produce a glassy groundmass, the results of an experimental study on the kinetics of sanidine crystallization by Fenn (1977) are applied to the experiments and natural sample investigated here. Fenn (1977) conducted a series of hydrous single-step cooling experiments on an ideal liquid ( $\text{Na}_{0.5}\text{K}_{0.5}\text{AlSi}_3\text{O}_8$ ) from above-liquidus conditions (i.e., no pre-existing crystals) and a range of water contents (2–12 wt%) and melt viscosities (3.2–8.9 log<sub>10</sub> Pa·s; calculated with Hui and

Zhang 2007). The experimental results of Fenn (1977) are presented as a function of their position beneath the liquidus, known as the degree of undercooling ( $\Delta T$ ). The degree of undercooling is defined as the difference between the temperature of the melt (or experiment) and the temperature of the mineral-in curve ( $T_{\text{melt/experiment}} - T_{\text{liquidus}}$ ) at a given pressure. Each position beneath the mineral-in curve (i.e.,  $\Delta T$  value) also has an associated equilibrium degree of crystallization; positions farthest away from a mineral-in curve have the greatest values of  $\Delta T$  and correspond to the most crystal-rich equilibrium conditions.

For decompressions, the effective undercooling ( $\Delta T_{\text{eff}}$ ) describes the position beneath the liquidus (as in Hammer and Rutherford 2002) (i.e., Fig. 6a). At a fixed temperature (i.e., 700 °C), values of  $\Delta T_{\text{eff}}$  increase as pressure decreases (Fig. 6b). Because  $P_{\text{Total}} = P_{\text{H}_2\text{O}}$ , decreases in pressure correspond to decreases in H<sub>2</sub>O contents (i.e., Fig. 6b), suggesting that progressive degassing also leads to a progressive increase in the degree of undercooling. Degassing to subliquidus conditions generates an undercooling and provides a powerful driver for crystallization; once a melt begins to crystallize, the  $\Delta T_{\text{eff}}$  value progressively decreases, and when equilibrium crystallinity is reached, then  $\Delta T_{\text{eff}} = 0$  °C (Hammer and Rutherford 2002; Couch et al. 2003; Brugger and Hammer 2010).

An outstanding question is whether or not the results of the cooling experiments (cooling-induced crystallization) of Fenn (1977) are truly applicable to a discussion of the kinetics of degassing-induced crystallization. In a comparative study of cooling- and degassing-induced crystallization kinetics, Shea and Hammer (2013) present experiments where undercoolings ( $\Delta T \leq 155$  °C) are induced by degassing and cooling. The cooling and degassing experimental series have run products with plagioclase nucleation rates that are on the same order of magnitude, for a given degree of undercooling. The liquids studied in Shea and Hammer (2013) differ from the liquid here in that they are more mafic (basaltic andesite) and all experiments are initiated from below all mineral liquidus. However, the similarities in the degassing and cooling experiments of Shea and Hammer (2013) suggest that the results of Fenn (1977) may be used as a framework for a discussion of the effects of degassing on the crystallization kinetics of sanidine in the Glass Mountain obsidians.

Results of the phase equilibrium experiments and FTIR analyses of the groundmass glass demonstrate that the obsidian (GM-11) traversed a range of H<sub>2</sub>O contents from 6.2 to 0.12 wt% at a pre-eruptive temperature of ~700 °C. At these conditions, sanidine crystallization in the natural sample is directly comparable to experimental series conducted by Fenn (1977) at 6.2 and 2.8 wt% H<sub>2</sub>O. The sanidine-in curve is not well defined at H<sub>2</sub>O contents <3 wt% (e.g., Fig. 1), and therefore, the  $\Delta T_{\text{eff}}$  value achieved by the adiabatic ascent path (Fig. 6a) at 2.8 wt% H<sub>2</sub>O is estimated to be ~150 °C by using a best fit line for the  $\Delta T_{\text{eff}}$  values and H<sub>2</sub>O contents (i.e., Fig. 6b). While the diagram in Fig. 6a shows isothermal degassing, it is more likely that during decompression the melt experiences some degree of cooling due to both ascent along the adiabatic and diffusive, conductive cooling due to the surrounding country rock, suggesting that our estimates of  $\Delta T_{\text{eff}}$  values for the natural sample over the given range of H<sub>2</sub>O contents are underestimates as degassing progresses to lower pressures.

The results of the experimental series conducted at 6.2 and 2.8 wt% H<sub>2</sub>O by Fenn (1977) show that the number of nucleation sites is initially small at low  $\Delta T$  values and increases as  $\Delta T$  values increase (Fig. 6c). There are three important observations to be made from the results of Fenn (1977): (1) Experiments conducted at 6.2 wt% H<sub>2</sub>O have a maximum number of nucleation sites at a  $\Delta T$  of ~170 °C, whereas the experiments with 2.8 wt% H<sub>2</sub>O have a maximum number of nucleation sites at a higher  $\Delta T$  value (~400 °C). (2) The maximum value of sanidine number densities is significantly lower in the series conducted at 6.2 wt% than the series conducted at 2.8 wt% H<sub>2</sub>O. (3) The number of nucleation sites in the experiments with 6.2 wt% H<sub>2</sub>O gradually decreases after the peak at  $\Delta T$  values >170 °C. The  $\Delta T_{\text{eff}}$  values traversed by GM-11 are shown in Fig. 6c as a gray box, where the lowest  $\Delta T_{\text{eff}}$  value (0°) correspond to the 6.2 wt% H<sub>2</sub>O nucleation density curve (as the natural sample crosses the sanidine + quartz-in curve at ~6.2 wt% H<sub>2</sub>O at 700 °C; Fig. 2), and the highest  $\Delta T_{\text{eff}}$  value (150 °C) corresponds to the 2.8 wt% H<sub>2</sub>O nucleation density curve. In all cases, the  $\Delta T_{\text{eff}}$  values traversed by the natural sample fall within a region of low nucleation densities. The results in Fig. 6c suggest that sanidine nucleation densities will remain low as degassing continues (i.e., from 6.2 to 2.8 wt% H<sub>2</sub>O; Fig. 6c), due to the shift in position of the nucleation density peak to greater degrees of undercooling as melt H<sub>2</sub>O progressively decreases, and thus, degassing can effectively hinder extensive nucleation of sanidine crystals.

With respect to sanidine growth rates presented in Fenn (1977) (Fig. 6d), the peak in growth rate always occurs at a  $\Delta T$  value lower than the peak in nucleation density. This observation suggests that crystallization at  $\Delta T$  values lower than the peak nucleation density will be characterized by growth-dominated regimes. The range of  $\Delta T_{\text{eff}}$  values (0 to ~150 °C) during degassing of 6.2–2.8 wt% H<sub>2</sub>O at 700 °C (Fig. 6a) is also shown in Fig. 6d as a light gray box. Comparison of the range of  $\Delta T_{\text{eff}}$  values traversed by the natural sample during degassing of 6.2–2.8 wt% H<sub>2</sub>O with the nucleation density and growth rate curves defined by Fenn (1977) demonstrates that sanidine crystal growth remains in a zone characterized by low nucleation densities (Fig. 6c) and elevated growth rates (Fig. 6d). Therefore, degassing-induced crystallization has the potential to result in growth of small numbers of relatively large sanidine crystals.

#### *Can near-equilibrium sanidine compositions crystallize in non-equilibrium abundances?*

A still outstanding question is whether crystal compositions grown in the natural sample during a dynamic process like degassing will closely follow compositions grown in

the phase equilibrium experiments. To evaluate this question, we draw from the literature documenting the effects of cooling and degassing on rapidly grown mineral compositions. Experimental studies by Iezzi et al. (2014) and Mollo et al. (2011) evaluate the effect of cooling rate (0.125–30 °C/min) on plagioclase composition. In those experiments, plagioclase was grown in rapidly cooled liquids and occurs in a reduced abundance (when compared with equilibrium experiments) with compositions that do not track equilibrium values and reflect an increased uptake of incompatible elements. In contrast, Waters et al. (2015) document plagioclase compositions in continuous decompression experiments (0.1–0.8 MPa/h) and find that plagioclase occurs in reduced abundance (compared to equilibrium experiments) with compositions that do broadly track those grown in phase equilibrium experiment. These apparently conflicting results are resolved when evaluated in the context of melt viscosity.

Melt viscosity is one of the primary controls on the diffusivity of melt components and therefore is critical to monitor in the context of transport of crystal-forming components to the crystallization front. In dynamic (i.e., degassing or cooling) experiments, the change in melt viscosity with time is an important variable to monitor and can be used as a basis of comparison between studies. Using the whole rock composition and the viscosity model of Hui and Zhang (2007), the cooling rates (0.125–30 °C/min) used in the experiments of Iezzi et al. (2014) and Mollo et al. (2011) can be translated into terms of changes in melt viscosity with time ( $\Delta\eta/t$ ) of 0.33–10.6  $\log_{10}$  Pa-s/h. These values are underestimates, as the experiments also crystallize, resulting in liquids with a progressively evolving (i.e., increasing in  $\text{SiO}_2$ ) composition, further increasing viscosity. The decompression experiments that crystallized plagioclase in Waters et al. (2015) were conducted at 0.8 and 0.1 MPa/h and correspond to  $\Delta\eta/t$  values of 0.0005–0.0042  $\log_{10}$  Pa-s/h. The rate of change in melt viscosity in the experiments run by Waters et al. (2015) is at least three orders of magnitude slower than those of both Iezzi et al. (2014) and Mollo et al. (2011), which is likely the explanation for why Waters et al. (2015) observed near-equilibrium compositions in the experiments that crystallized, whereas Iezzi et al. (2014) and Mollo et al. (2015) observed disequilibrium compositions.

An additional factor that may control sanidine composition is the composition of the melt, and this effect can be evaluated using the glass compositions measured in the phase equilibrium experiments (Table 3). In the experiments conducted at 700 °C (i.e., G29, G10, G17, G19 and G27), the liquid compositions measured by microprobe change only slightly and major oxide components are often within  $2\sigma$  values of each other, yet sanidine composition changes from  $\text{Or}_{75}$  [G10; 200 MPa( $\text{P}_{\text{H}_2\text{O}}$ ) and 6.15 wt%  $\text{H}_2\text{O}$ ] to  $\text{Or}_{57}$  [G27;

100 MPa( $\text{P}_{\text{H}_2\text{O}}$ ) and 4.35 wt%  $\text{H}_2\text{O}$ ]. These results suggest that, for at least the experiments conducted at 700 °C, the wt%  $\text{H}_2\text{O}$  in equilibrium the liquid exerts a greater control over sanidine composition than the corresponding liquid composition, and therefore small changes in melt  $\text{H}_2\text{O}$  content exert a relatively large control over sanidine composition.

In the scenario of degassing-induced sanidine crystallization, it is possible for sanidine compositions to track dissolved melt  $\text{H}_2\text{O}$  provided that degassing occurs at slow rates (e.g., comparable to the rates in Waters et al. (2015) where crystallization occurred; 0.1–0.8 MPa/h). Rates of these magnitudes allow for equilibrium degassing of  $\text{H}_2\text{O}$  (Gardner et al. 1999; Larsen et al. 2004) and should allow ample time for crystallization of near-equilibrium compositions, given the sensitivity of sanidine composition to wt%  $\text{H}_2\text{O}$  in the melt and the requirement of simultaneous non-explosive degassing for obsidian eruption. An important point that must be made here is that the decompression rates that allow for crystallization of near-equilibrium compositions are slow. When these slow decompression rates (i.e.,  $\leq 0.8$  MPa/h) are utilized in experiments that are initiated below the liquidus, the run products are consistently crystal rich (e.g., Brugger and Hammer 2010). Therefore, in order for sanidine crystals to have compositions to track dissolved melt  $\text{H}_2\text{O}$  and occur in a remarkably sparse abundance, GM-11 must have initiated decompression and degassing from above-liquidus conditions.

#### *Can degassing-induced crystallization produce the granophyric textures and melt boundary layers?*

The last open question is whether degassing can generate the granophyric textures and the boundary layers mantling sanidine in the natural sample (Fig. 1). Central to the preceding points is the importance of decompression-induced degassing without any nucleation sites or crystals present in the melt, so nucleation is suppressed and crystallization is effectively inhibited. Sanidine grown in the run product of the single-step decompression experiment has a granophyric texture, characterized by intergrowths of quartz in the sanidine lattice (Fig. 4). Growth of plagioclase occurs on the margins of sanidine crystals, which is similar to the texture observed in the natural sample (Fig. 1). The granophyric texture in the natural sample suggests that there are limited or no nucleation sites present at the time of crystal growth and that quartz nucleates on the available sanidine surface. This is confirmed by sanidine growth with granophyric texture in the run products of the decompression experiment, where decompression is initiated from superheated conditions. The decompression experiment differs from the natural sample in that it achieved an equilibrium degree of crystallinity in nine days, as suggested by the glass composition and the degree of crystallinity

estimated from BSE images (Table 3), and in no instance did an obvious boundary layer develop around crystals of sanidine. The absence of this melt boundary layer in the single-step decompression implies that crystallization in the natural sample occurred during a dynamic process like degassing, as a scenario where steady-state conditions are achieved (i.e., the decompression experiment; Fig. 5) will allow for crystallization followed by re-equilibration of any existing melt boundary layer with surrounding melt. In contrast, sanidine crystallization in the natural sample must have occurred relatively rapidly to generate a melt boundary layer (due to elevated crystal growth rates; Fig. 6), followed shortly thereafter by eruption to prevent diffusive re-equilibration of that boundary layer with the surrounding melt.

### Summary

Evidence from results presented here and from the experimental literature strongly suggests that degassing has the potential to (1) restrict extensive crystallization, (2) inhibit nucleation, (3) induce crystallization of sanidine with compositions that record changing water contents, provided degassing initiates from above-liquidus conditions, and (4) produce sanidine with granophyric textures. Common to all of these points is the underlying importance that decompression-induced degassing initiates from crystal- and nuclei-free (superheated) conditions to retard crystallization, suppress extensive nucleation and remain in a growth-dominated regime (i.e., Fenn 1977; Fig. 6). Moreover, initiating decompression and degassing from superheated conditions at effusive speeds (e.g.,  $<2.2$  MPa/h; Castro and Gardner 2008) allows sanidine to maintain near-equilibrium compositions (i.e., those that track compositions grown in phase equilibrium experiments) and develop melt boundary layers as crystallization outcompetes melt diffusion due to rapidly changing melt viscosity. The hypothesis could be posed that the rhyolite melts that formed the Glass Mountain obsidians were efficiently segregated melts from the position on the  $H_2O$ -saturated phase diagram (Fig. 2) where all the major mineral phases are in equilibrium [i.e.,  $\leq 725$  °C and  $<130$  MPa( $P_{H_2O}$ )]. However, fluid-saturated melts that segregate from those conditions will contain abundant nucleation sites and subsequent decompression will necessarily induce extensive crystallization, as demonstrated by many experimental studies (Geschwind and Rutherford 1995; Hammer and Rutherford 2002; Couch et al. 2003; Martel and Schmidt 2003; Brugger and Hammer 2010), prohibiting the effusive eruption of a liquid consisting of mostly glass with negligible crystallization (i.e., obsidian). Superheating inhibits extensive crystallization (by eliminating nucleation sites) during effusive (slow) eruption resulting in glassy, crystal-poor lavas, thereby resolving a paradox unique to obsidians.

### Superheating and the formation of Glass Mountain obsidian

Given the importance of superheating in the formation of GM-11, it is important to consider the conditions in nature where superheating occurs. The mechanisms that can cause superheating are (1) wholesale melting and (2) fluid under-saturated decompression of an interstitial melt (see schematic Fig. DR-4). Wholesale melting of a pre-existing lithology (i.e., heating to above-liquidus conditions) will efficiently purge the melt of all existing nuclei and crystals, in the presence or absence of a co-existing vapor phase (i.e., fluid-saturated or fluid under-saturated conditions). Alternatively, in the scenario where superheating is achieved through decompression, the melt must initially be fluid under-saturated. In the absence of a fluid phase, high pressures generally stabilize smaller volume, crystalline phases and low pressures stabilize the larger volume, melt phase (for a given temperature). Therefore, isothermal decompression of a fluid under-saturated interstitial melt would move it from a position of crystalline stability to a position where only melt is stable (i.e., superliquidus or superheated conditions). After extraction, decompression and subsequent superheating of the interstitial melts occur, those melts may reach fluid saturation, and eventually degassing-induced crystallization may proceed. While the results of this study define the pre-eruptive, pre-crystallization histories of the Glass Mountain obsidians by identifying two scenarios where superheating may occur (wholesale melting or fluid under-saturated decompression), the kinetic results alone do not place any constraint on the processes by which the melts form (i.e., partial melting, cooling/crystallization or wholesale melting). To further constrain the processes by which the melts form, the kinetic results are applied to isotopic studies previously conducted on the Glass Mountain lavas.

On the basis of isotopic and geochemical data (Metz and Mahood 1991; Halliday et al. 1989; Davies et al. 1994), Hildreth (2004) proposed that the Glass Mountain obsidians represent the early-erupted melts that form the silica-rich and crystal-poor cap of a large-volume rhyolitic magma system. The eruption of these melts is followed by the large-volume eruption of the underlying crystal-rich mushy magma ( $>50$  % phenocrysts) (i.e., Late Bishop Tuff). In this model, the Glass Mountain obsidians are genetically related to the Bishop Tuff magmatic reservoir. If the Glass Mountain obsidians are indeed interstitial melts derived from the Bishop Tuff magmatic system, the large-volume reservoir is required to be fluid under-saturated to enable the rhyolite melts (i.e., Glass Mountain obsidians) to undergo an interval of superheating upon initial extraction, ascent and degassing, so that they erupt as obsidians. Similarly, if the Glass Mountain obsidians represent the



interstitial partial melts of granitoid lithologies, as proposed by Sparks et al. (1990), those melts are also required to initially be fluid under-saturated so that superheating is achieved upon decompression. Alternatively, if the Glass Mountain obsidians formed in the presence of a co-existing fluid phase, the only mechanism that can generate an interval of superheating is wholesale melting. Mahood (1990) presents a model in which the Glass Mountain obsidians are derived via wholesale melting of leucocratic granites, which could plausibly explain the similarities in major, trace element compositions and variations isotopes between the Glass Mountain obsidians.

While these results do not uniquely support a single proposed mechanism for the genesis of Glass Mountain obsidians, they provide constraints on the presence or absence of a vapor phase in each of the scenarios, which aids in limiting the possible mechanisms by which the Glass Mountain liquids are separated from their crystal-rich sources. For those scenarios that require superheating by fluid under-saturation (where Glass Mountain lavas are interstitial melts formed by either partial melting or as the residual liquids of a crystallizing mush), gas-driven filter pressing (Sisson and Bacon 1999; Pistone et al. 2015) must be eliminated as the method of melt extraction from a crystalline cumulate for obsidian lavas, as this process fundamentally requires fluid saturation and an interval of superheating would not be achieved, resulting in extensive crystallization of the melt.

## Conclusions

Comparison of sanidine compositions in the natural liquid with those grown in a series of phase equilibrium experiments demonstrates that sanidine within Glass Mountain obsidian GM-11 crystallized in response to degassing. We find that degassing can explain four characteristics unique to the sanidine crystals the GM-11 obsidian, provided that the liquid has undergone a period of superheating. (1) Comparison of the starting conditions of experiments documenting the kinetics of degassing-induced crystallization in rhyolite liquids demonstrates that degassing has the potential to sufficiently inhibit crystallization in the Glass Mountain obsidians, provided that decompression be induced from superliquidus conditions. (2) Evaluation of the effects of H<sub>2</sub>O on sanidine nucleation and growth rates using an experimental study from the literature suggests that degassing may sufficiently inhibit extensive nucleation in the Glass Mountain obsidians due to shifting the maximum values of nucleation densities to increasingly greater degrees of undercooling. (3) It is possible for near-equilibrium sanidine compositions to form in non-equilibrium abundances in the Glass Mountain obsidians given the potent effect of H<sub>2</sub>O (rather than melt composition) on sanidine composition and provided

that decompression occurs at rates that permit equilibrium degassing and ample time for adequate diffusion of melt components. (4) The unique granophyric texture was replicated in the decompression experiments initiated from superliquidus conditions, which suggests that the granophyric texture in the Glass Mountain obsidians forms in scenarios where nucleation sites are sparse. The distinctive melt boundary layers mantling sanidine suggest that crystallization in the natural sample occurred during a dynamic process like decompression-induced degassing in a timescale too short to permit diffusive re-equilibration of the boundary layer with the surrounding melt. Our data from both natural and experimental observations suggest that in order for sanidine to grow during degassing, and for rhyolite liquids to erupt effusively (slowly) in the absence of extensive crystallization, an interval of superheating is required prior to decompression.

Pre-existing geochemical and isotopic work in the literature suggests that the Glass Mountain lavas may have origins as the interstitial melts of an extensively crystallized volume of magma, the interstitial melts of partially melting plutons, or wholesale melts. Our results further constrain each of these models for the origins of the Glass Mountain obsidians by identifying the scenarios that require the absence of a fluid phase to achieve superheating (fluid under-saturated decompression or wholesale melting) and the scenarios where superheating is achieved in the presence of a fluid phase (wholesale melting).

By assigning the presence or absence of a fluid phase to these scenarios, our results also help to eliminate extraction methods for these crystal-poor obsidians from their respective sources. For any scenario where fluid under-saturation is required, gas-driven filter pressing is eliminated as a mechanism of melt extraction for obsidians.

**Acknowledgments** Stephanie Grocke is thanked for extensive discussion and feedback on this manuscript. Gail Mahood is thanked for lively discussion and feedback following presentation of this paper at AGU 2015. Silvio Mollo, Matteo Masotta and an anonymous third and fourth reviewers are sincerely thanked for extensive, constructive feedback, which significantly improved this manuscript. Becky Lange, James Jolles and John Naliboff are additionally thanked for assistance with field work. Funding for this work was provided by the Smithsonian Institution National Museum of Natural History Peter S. Buck Postdoctoral Scholarship Program.

## References

- Almeev RR, Bolte T, Nash BP, Holtz F, Erdmann M, Cathey H (2012) High-temperature, low-H<sub>2</sub>O silicic magmas of the Yellowstone Hotspot: an Experimental Study of Rhyolite from the Bruneau-Jarbidge Eruptive Center, Central Snake River Plain, USA. *J Petrol* 53:1837–1866
- Anderson AT, Davis AM, Lu F (2000) Evolution of bishop tuff rhyolitic magma based on melt and magnetite inclusions and zoned phenocrysts. *J Petrol* 41:449–473

- Andújar J, Scaillet B (2012a) Experimental constraints on parameters controlling the difference in the eruptive dynamics of phonolitic magmas: the case of Tenerife (Canary Islands). *J Petrol* 53:1777–1806
- Andújar J, Scaillet B (2012b) Relationships between pre-eruptive conditions and eruptive styles of phonolite-trachyte magmas. *Lithos* 152:122–131
- Andújar J, Costa F, Martí J, Wolff JA, Carroll MR (2008) Experimental constraints on pre-eruptive conditions of phonolitic magma from the caldera-forming El Abrigo eruption, Tenerife (Canary Islands). *Chem Geology* 257(173):191
- Bailey RA (1989) Geologic map of the Long Valley caldera, Mono-Inyo-Craters volcanic chain, and vicinity, eastern California. US Geol Surv Map I-1933 scale 1:62,500; pamphlet
- Befus KS, Gardner JE (2016) Magma storage and evolution of the most recent effusive and explosive eruptions from the Yellowstone Caldera. *Contrib Mineral Petrol* 171:30
- Brugger CR, Hammer JE (2010) Crystallization kinetics in continuous decompression experiments: implications for interpreting natural magma ascent processes. *J Petrol* 51:1941–1965
- Buddington AF, Lindsley D (1964) Iron-titanium oxide minerals and synthetic equivalents. *J Petrol* 5:310–357
- Carmichael ISE (1967) The Fe-Ti oxides of silic volcanic rocks and their associated ferromagnesian silicates. *Contrib Mineral Petrol* 14:36–64
- Castro JM, Gardner JE (2008) Did magma ascent rate control the explosive-effusive transition at the Inyo volcanic chain, California? *Geology* 36:279–282
- Couch S, Sparks RSJ, Carroll MR (2003) The kinetics of degassing-induced crystallization at Soufriere Hills Volcano, Montserrat. *J Petrol* 44:1477–1502
- Davies GR, Halliday AN, Mahood GA, Hall CM (1994) Isotopic constraints on the production rates, crystallization histories and residence time of pre-caldera silicic magmas Long Valley, California. *Earth Planet Sci Lett* 125:17–37
- Fabbrizio A, Carroll MR (2008) Experimental constraints on the differentiation process and pre-eruptive conditions in the magmatic system of Phlegraean Fields (Naples, Italy). *J Volc Geotherm Res* 171:88–102
- Fabbrizio A, Scaillet B, Carroll MR (2009) Estimation of pre-eruptive magmatic water fugacity in the Phlegraean Fields, Naples, Italy. *European J Mineral* 21:107–116
- Fenn PM (1977) The nucleation and growth of alkali feldspars from hydrous melts. *Can Mineral* 15:135–161
- Gardner JE, Hilton M, Carrol MR (1999) Experimental constraints on degassing of magma: isothermal bubble growth during continuous decompression from high pressure. *Earth Planet Sci Lett* 168:201–218
- Gardner JE, Befus KS, Gualda GAR, Ghiorso MS (2014) Experimental constraints on rhyolite-Melts and the Late Bishop Tuff magma body. *Contrib Mineral Petrol* 168:1051
- Geschwind CH, Rutherford M (1995) Crystallization of microlites during magma ascent: the fluid mechanics of 1980–1986 eruptions at Mount St Helens. *Bull Volc* 57:356–370
- Ghiorso M, Evans BW (2008) Thermodynamics of rhombohedral oxide solid solutions and a revision of the Fe-Ti two-oxide geothermometer and oxygen barometer. *Am J Sci* 308:957–1039
- Halliday AN, Mahood GA, Hotden P, Mctz JM, Dempster TJ, Davidson JP (1989) Evidence for long residence times of rhyolitic magma in the Long Valley magmatic system: the isotopic record in precaldere lavas of Glass Mountain. *Earth Planet Sci Lett* 94:274–290
- Hammer JE, Rutherford MJ (2002) An experimental study of the kinetics of decompression-induced crystallization in silicic melt. *J Geophys Res* 107(B1):2021
- Hildreth W (1977) The magma chamber of the Bishop Tuff: gradients in temperature, pressure, and composition. Ph.D. thesis, University of California, Berkeley
- Hildreth W (1979) The Bishop Tuff: evidence for the origin of compositional zonation in silicic magma chambers. In: Chapin CE, Elston WE (eds) *Ash-Flow Tuffs*. Geol. Soc. Am. Spec. Pap. vol 180, pp 43–75
- Hildreth W (2004) Volcanological perspectives on Long Valley, Mammoth Mountain and Mono Craters: several contiguous but discrete systems. *J Volc Geotherm Res* 136:169–198
- Hildreth W, Wilson CNJ (2007) Compositional Zoning of the Bishop Tuff. *J Petrol* 48:951–999
- Housh TB, Luhr JF (1991) Plagioclase-melt equilibria in hydrous systems. *Am Mineral* 76:477–492
- Hui N, Zhang Y (2007) Toward a general viscosity equation for natural anhydrous and hydrous silicate melts. *Geochim Cosmochim Acta* 71:403–416
- Iezzi G, Mollo S, Torresi G, Ventura G, Cavallo A, Scarlato P (2011) Experimental solidification of an andesitic melt by cooling. *Chem Geology* 283:261–273
- Iezzi G, Mollo S, Shahini E, Cavallo A, Scarlato P (2014) The cooling kinetics of plagioclase feldspar as revealed by electron-microprobe mapping. *Am Mineral* 99:898–907
- Lange RA, Frey HM, Hector J (2009) A thermodynamic model for the plagioclase-liquid hygrometer/thermometer. *Am Mineral* 94:494–506
- Larsen JF, Denis MH, Gardner JE (2004) An experimental study of bubble coalescence in rhyolitic and phonolitic melts. *Geochim Cosmochim Acta* 68:333–344
- Leschik M, Heide G, Frischat GH, Behrens H, Wiedenbeck M, Wagner N, Heide K, Geißler H, Reinholz U (2004) Determination of H<sub>2</sub>O and D<sub>2</sub>O contents in rhyolitic glasses using KFT, NRA, EGA, IR spectroscopy, and SIMS. *Phys Chem Glasses* 45:238–251
- Liu Y, Zhang Y, Behrens H (2005) Solubility of H<sub>2</sub>O in rhyolitic melts at low pressure and a new empirical model for mixed H<sub>2</sub>O-CO<sub>2</sub> solubility in rhyolitic melts. *J Volcanol Geotherm Res* 143:219–235
- Mahood GA (1990) A second reply to “Comments by R.S.J. Sparks, H.E. Huppert, and C.J.N. Wilson on “Evidence for long residence times of rhyolitic magma in the Long Valley magmatic system: the isotopic record in the precaldere lavas of Glass Mountain”. *Earth Planet Sci Lett* 99:395–399
- Mankinen EA, Gromme CS, Dalrymple GB, Lanphere MA, Bailey RA (1986) Paleomagnetism and K-Ar ages of volcanic rocks from Long Valley caldera, California. *J Geophys Res* 91:633–652
- Martel C (2012) Eruption dynamics inferred from microlite crystallization experiments: application to Plinian and dome-forming eruptions of Mt Pelée (Martinique, Lesser Antilles). *J Petrol* 53:699–725
- Martel C, Schmidt BC (2003) Decompression experiments as an insight into ascent rates of silicic magmas. *Contrib Mineral Petrol* 144:397–415
- Martel C, Champallier R, Prouteau G, Pichavant M, Arbaret L, Balcone-Boissard H, Boudon G, Boivin P, Bourdier J, Scaillet B (2013) Trachyte phase relations and implication for magma storage conditions in the chaîne des puys (French Massif Central). *J of Petrol* 54:1071–1107
- Metz JM, Bailey RA (1993) Geologic map of Glass Mountain, Mono County, California. U.S. Geol. Surv. Map I-1995, scale 1:24,000
- Metz JM, Mahood GA (1985) Precursors to the bishop tuff eruption: glass mountain, Long Valley, California. *J Geophys Res* 90:11121–11126
- Metz JM, Mahood GA (1991) Development of the Long Valley, California, magma chamber recorded in precaldere rhyolite lavas of Glass Mountain. *Contrib Mineral Petrol* 106:379–397
- Mollard E, Martel C, Bourdier JL (2012) Decompression-induced crystallization in hydrated silica-rich melts: empirical models of experimental plagioclase nucleation and growth kinetics. *J Petrol* 53:1743–1766

- Mollo S, Putirka K, Iezzi G, Del Gaudio P, Scarlato P (2011) Plagioclase-melt (dis)equilibrium due to cooling dynamics: implications for thermometry, barometry and hygrometry. *Lithos* 125:221–235
- Mollo S, Masotta M, Forni F, Bachmann O, De Astis G, Moore G, Scarlato P (2015) A K-feldspar–liquid hygrometer specific to alkaline differentiated magmas. *Chemical Geology* 392:1–8
- Pistone M, Arzilli F, Dobson KJ, Cordonnier B, Reusser E, Ulmer P, Marone F, Whittington AG, Mancini L, Fife JL, Blundy JD (2015) Gas-driven filter pressing in magmas: insights into in situ melt segregation from crystal mushes. *Geology* 43:699–702
- Putirka KD (2005) Igneous thermometers and barometers based on plagioclase + liquid equilibria: tests of some existing models and new calibrations. *Am Mineral* 90:336–346
- Scaillet B, MacDonald R (2001) Phase relations of peralkaline silicic magmas and petrogenetic implications. *J Petrol* 42:825–845
- Scaillet B, Macdonald R (2003) Experimental constraints on the relationships between Peralkaline Rhyolites of the Kenya rift valley. *J Petrol* 44:1867–1894
- Shea T, Hammer JE (2013) Kinetics of cooling- and decompression-induced crystallization in hydrous mafic-intermediate magmas. *J Volc Geotherm Res* 260:127–145
- Simon JJ, Reid MR (2005) The pace of rhyolite differentiation and storage in an “archetypical” silicic magma system, Long Valley, California. *Earth Planet Sci Lett* 235:123–140
- Sisson TW, Bacon CR (1999) Gas-driven filter pressing in magmas. *Geology* 27:613–616
- Sparks RSJ, Huppert HE, Wilson CJN (1990) Comment on ‘Evidence for long residence times of rhyolitic magma in the Long Valley magmatic system: the isotopic record in precaldera lavas of Glass Mountain’ by Halliday A.N., Mahood G.A., Holden P., Metz J.M., Dempster, T.J. and Davidson J.P. *Earth Planet Sci Lett* 99:387–389
- Venezky DY, Rutherford MJ (1999) Petrology and Fe-Ti oxide reequilibration of the 1991 Mount Unzen mixed magma. *J Volc Geotherm Res* 89:213–230
- Vetere F, Iezzi G, Behrens H, Cavallo A, Misiti V, Dietrich M, Knipping J, Ventura G, Mollo S (2013) Intrinsic solidification behavior of basaltic to rhyolitic melts: a cooling rate experimental study. *Chem Geology* 354:233–242
- Wallace PJ, Anderson AT, Davis AM (1999) Gradients in H<sub>2</sub>O, CO<sub>2</sub>, and exsolved gas in a large-volume silicic magmas system: interpreting the record preserved in melt inclusions from the Bishop Tuff. *J Geophys Res* 104:97–122
- Waters LE, Lange RA (2013) Crystal-poor, multiply saturated rhyolite (obsidians) from the Cascade and Mexican arcs: evidence of degassing-induced crystallization of phenocrysts. *Contrib Mineral Petrol* 166:731–754
- Waters LE, Andrews BJ, Lange RA (2015) Degassing-induced crystallization of plagioclase phenocrysts in rhyolite and dacite: phase equilibrium and decompression experiments. *J Petrol* 56:981–1006
- Zhang Y, Xu Z, Zhu M, Wang H (2007) Silicate melt properties and volcanic eruptions. *R Geophys* 45:RG4004